

Amplitude Expansion Phase Field Crystal (APFC) Modeling based Efficient Dislocation Simulations using Fourier Pseudospectral Method

Xinyi Wei¹, Yangshuai Wang², Kai Jiang^{3,*}, and Lei Zhang^{1,*},

¹ *School of Mathematical Sciences, Institute of Natural Sciences and MOE-LSC, Shanghai Jiao Tong University, Shanghai 200240, China.*

² *Department of Mathematics, Faculty of Science, National University of Singapore, 10 Lower Kent Ridge Road, Singapore.*

³ *Hunan Key Laboratory for Computation and Simulation in Science and Engineering, Key Laboratory of Intelligent Computing and Information Processing of Ministry of Education, School of Mathematics and Computational Science, Xiangtan University, Xiangtan, Hunan, 411105, China.*

Abstract. Crystalline defects play a critical role in determining the properties of crystalline solids, underscoring the need for accurate computational methods to study them. Lattice deformation in dislocation simulations, which involves changes in atomic positions, can be described either microscopically by specific atomic configurations or macroscopically by continuum elasticity, each with inherent limitations. The complex amplitude expansion of the phase field crystal (APFC) model provides a mesoscopic approach that bridges these scales. In this paper, we introduce a Fourier pseudospectral method for efficiently solving the APFC model in the context of crystalline defect simulations. This study marks the first application of the Fourier pseudospectral method to the APFC model. The method fully exploits the system's periodicity and facilitates the implementation of periodic boundary conditions, thanks to its high accuracy and computational efficiency. Numerical experiments conducted on two-dimensional triangular lattices and three-dimensional body-centered cubic lattices for edge dislocation geometry optimization have produced strain field images that align well with by continuum elasticity predictions. The findings demonstrate the potential of the APFC model to accurately capture the complex strain fields associated with dislocations at the mesoscopic scales, a key step toward modeling more intricate crystalline defect structures and dynamics.

AMS subject classifications: 52B10, 65D18, 68U05, 68U07

Key words: crystal defects, amplitude expansion, phase field crystal model, Fourier pseudospectral method, elastic strain field

*Corresponding author. *Email addresses:* xinyiwei@sjtu.edu.cn (X. Wei), yswang@nus.edu.sg (Y. Wang), kaijiang@xtu.edu.cn (K. Jiang), lzhang2012@sjtu.edu.cn (L. Zhang)

*Corresponding author. *Email addresses:* xinyiwei@sjtu.edu.cn (X. Wei), yswang@nus.edu.sg (Y. Wang), kaijiang@xtu.edu.cn (K. Jiang), lzhang2012@sjtu.edu.cn (L. Zhang)

1 Introduction

Crystalline defects, including point defects, dislocations, and cracks, significantly influence the properties of crystalline solids [1–5]. Accurate and efficient computational methods are crucial for studying these defects, particularly dislocations, which are key to understanding material behavior. While microscopic simulations are often computationally intensive and macroscopic models may lack precision, mesoscopic approaches strike an effective balance by offering coarse-grained degrees of freedom that enhance computational efficiency while maintaining sufficient accuracy, making them especially suitable for dislocation simulations. Prominent mesoscopic models include discrete dislocation dynamics (DDD) [6, 7], coarse-grained molecular dynamics (CGMD) [8, 9], kinetic Monte Carlo (kMC) [10, 11], and phase field crystals (PFC) [12–15].

The PFC model excels in describing changes in the free energy functional with respect to local atomistic density, providing valuable insights into elasticity and dislocation dynamics. However, its application is limited by the need for fine spatial discretization. To address this, Goldenfeld et al. [16] introduced the complex amplitude expansion of the PFC (APFC) model. This extension, based on the plane wave expansion of the density, allows for the exploration of longer time scales and larger length scales, significantly broadening the model’s applicability in advanced material modeling [17–20]. The APFC model is particularly useful for studying elastic effects [20, 21], dislocation dynamics [22, 23], and the control of material properties [24, 25]. It can be effectively applied across various atomic descriptions, including those from theoretical modeling [26], atomic simulations [27], and experimental imaging [20].

The primary challenge in APFC models lies in the development and implementation of efficient numerical algorithms, particularly for dislocation simulations, which are crucial in computational materials science. The model is nonlinear with higher-order terms, and the corresponding dynamic equations involve multiple amplitude functions associated with reciprocal lattice vectors. Various numerical methodologies have been proposed to solve the APFC model. The finite difference method was initially employed [16, 28], but it suffered from instability issues, requiring constraints on the time step due to grid spacing limitations [29]. To address this difficulty, semi-implicit methods and spatial adaptivity have been explored. For example, finite element method [24, 30–33] and Fourier spectral method [34, 35] have been utilized for APFC models. However, finite element methods may not optimally exploit the periodic lattice structures in crystal models. While the Fourier spectral method offers a global representation through Fourier series, it can result in increased free energy if the time step is too large for certain models [36]. Additionally, efficiency remains a concern across these approaches. Therefore, further research is required to comprehensively address these challenges.

The Fourier pseudospectral method [37, 38], closely related to the Fourier spectral method, solves PDEs at collocation points in physical space rather than solving the variational problem. This simplifies the treatment of nonlinear terms and facilitates the evaluation of certain operators. By leveraging fast algorithms like the fast Fourier transform, it significantly accelerates calculations, scaling as $O(N \log N)$, where N represents

the number of degrees of freedom. In this paper, we utilize the Fourier pseudospectral method in the spatial domain to fully exploit the periodicity inherent in crystalline structure while enhancing computational efficiency, combined with a semi-implicit discrete scheme for time integration. Our numerical experiments showcase edge dislocations in two-dimensional triangular and three-dimensional body-centered cubic (BCC) lattices. With a careful choice of the initial guess, we solve the APFC model equations using the Fourier pseudospectral method to approximate the amplitude functions. From these solutions, we compute the order parameter and strain field, achieving a distribution consistent with theoretical predictions. Additionally, we analyze the decay of the strain field along a specific direction over a large area, comparing it with standard continuum elasticity theory [39].

This paper primarily focuses on applying the Fourier pseudospectral method within the APFC model to simulate dislocations, highlighting its potential and advantages in solving periodic crystalline defect systems. However, the proposed analysis and methodology can also be extended to grain boundaries and other complex scenarios. We plan to explore the generalization of these approaches in future research and discuss potential developments in Section 5.

Outline:

This paper is organized as follows: Section 2 introduces the APFC model and the lattice configurations required for numerical simulations. Section 3 details the Fourier pseudospectral method, including its formulation and the effective implementation for solving the APFC model. Section 4 presents numerical results for edge dislocations in both two-dimensional triangular and three-dimensional body-centered cubic lattices, with analysis and interpretation within the context of the APFC model. Section 5 summarizes the key findings and outlines future research directions. The appendices provide supplementary information for interested readers.

2 APFC Model

In this section, we provide a derivation of the APFC model from the PFC free energy functional, as well as the corresponding evolution equations for the crystalline lattices considered in this work. The PFC free energy functional [12–15] is defined with respect to the dimensionless atomic probability density n , which serves as a continuum representation of discrete atomic lattices. The functional is given by,

$$F_n = \frac{1}{|\Omega|} \int_{\Omega} \left[\frac{B_0}{2} n^2 + \frac{B_x}{2} n(1 + \nabla^2)^2 n - \frac{\tau}{3} n^3 + \frac{v}{4} n^4 \right] d\mathbf{r}, \quad (2.1)$$

where Ω is the computational domain and B_x, v, τ and B_0 are parameters that control the phase diagram and properties of underlying system [40]. The amplitude expansion based PFC (APFC) model [16, 41, 42] can be derived by incorporating crystalline information

and approximating the density n as a sum of plane waves

$$n(\mathbf{r}) = n_0(\mathbf{r}) + \sum_{j=1}^N [\eta_j(\mathbf{r}) e^{i\mathbf{k}_j \cdot \mathbf{r}} + \eta_j^*(\mathbf{r}) e^{-i\mathbf{k}_j \cdot \mathbf{r}}]. \quad (2.2)$$

The set $\{\mathbf{k}_j\}_{j=1}^N$ consists of N non-zero reciprocal lattice vectors that represent distinct lattice symmetries, defined as $\mathbf{k}_j = \sum_{i=1}^N n_i \mathbf{b}_i$, where \mathbf{b}_j are the primitive reciprocal lattice vectors and $n_i \in \mathbb{Z}$ are their coefficients. They satisfy the relation $\mathbf{a}_i \cdot \mathbf{b}_j = 2\pi \delta_{ij}$, with \mathbf{a}_i being the primitive vectors of the crystal lattice [43]. The variables $\eta_j(\mathbf{r})$ are amplitude functions corresponding to each plane wave, which are crucial for characterizing the state and evolution of the crystal system. Without loss of generality, the average density $n_0(\mathbf{r})$ can be set to zero [20]. We will illustrate two specific examples at the end of this section (cf. Example 2.1).

In the PFC model, the density n satisfies the following dynamic equation, which represents a gradient flow of the energy functional,

$$\frac{\partial n}{\partial t} = \nabla^2 \frac{\delta F_n}{\delta n}, \quad (2.3)$$

where

$$\frac{\delta F_n}{\delta n} = B_0 n + B_x (1 + \nabla^2)^2 n - \tau n^2 + v n^3. \quad (2.4)$$

In the following, we derive the dynamic equation within the APFC framework.

QDRG argument By applying the ∇^2 operator to n and using (2.2), we obtain the following result,

$$\nabla^2 n = \sum_j e^{i\mathbf{k}_j \cdot \mathbf{r}} (\nabla^2 + 2i\mathbf{k}_j \cdot \nabla - |\mathbf{k}_j|^2) \eta_j + \sum_j e^{-i\mathbf{k}_j \cdot \mathbf{r}} (\nabla^2 + 2i\mathbf{k}_j \cdot \nabla - |\mathbf{k}_j|^2) \eta_j^*, \quad (2.5)$$

We then utilize the “quick and dirty renormalization group” (QDRG) approach proposed by [42] to capture the essential aspects of the calculations without relying on more rigorous methods. The main idea is to assume that the amplitudes $\eta_j(\mathbf{r})$ remain constant on atomic length scales. As discussed in Remark 2.1, and demonstrated in the corresponding proof in Appendix B.3, we obtain

$$\int_{C_1} \eta_j(\mathbf{r}) e^{i\mathbf{k}_j \cdot \mathbf{r}} d\mathbf{r} \approx \eta_j(\mathbf{r}) \int_{C_1} e^{i\mathbf{k}_j \cdot \mathbf{r}} d\mathbf{r}, \quad (2.6)$$

where C_1 is the unit cell. Since $e^{i\mathbf{k}_j \cdot \mathbf{r}}$ is periodic in the crystal cell, the right hand side of equation (2.6) vanishes unless $\mathbf{k}_j = 0$.

Remark 2.1. To prove (2.6), we consider the integral of its left-hand side over the cell C_ε with $\varepsilon > 0$. The following formula holds:

$$\left| \frac{1}{\varepsilon^d} \int_{C_\varepsilon} \eta(\mathbf{x}) e^{i\mathbf{k}_j \cdot \frac{\mathbf{x}}{\varepsilon}} d\mathbf{x} - \frac{1}{\varepsilon^d} \int_{C_\varepsilon} I_\eta e^{i\mathbf{k}_j \cdot \frac{\mathbf{x}}{\varepsilon}} d\mathbf{x} \right| = O(\varepsilon), \quad (2.7)$$

where

$$I_\eta = \frac{1}{\varepsilon^d} \int_{C_\varepsilon} \eta(\mathbf{x}) d\mathbf{x} \quad (2.8)$$

represents the average value of the integral of $\eta(\mathbf{x})$ over C_ε . Here, ε^d denotes the volume of the C_ε cell, and d is the dimension of the model. The complete proof is given in Appendix B.3.

Dynamic equation of amplitude functions In the APFC framework, the dynamic equation for the density n given by (2.3) is transformed into a dynamic equation for the amplitude functions η_j . This is achieved by multiplying the left-hand side of (2.3) by $e^{-i\mathbf{k}_j \cdot \mathbf{r}}$, integrating over a unit cell C_0 , and normalizing by its volume $|C_0|$. By applying the QDRG approach, we can obtain,

$$\frac{1}{|C_0|} \int_{C_0} e^{-i\mathbf{k}_j \cdot \mathbf{r}} \cdot \frac{\partial n}{\partial t} d\mathbf{r} = \frac{1}{|C_0|} \int_{C_0} \frac{\partial \eta_j}{\partial t} + \sum_{\substack{l=1 \\ l \neq j}}^N \frac{\partial(\eta_l e^{i(\mathbf{k}_l - \mathbf{k}_j) \cdot \mathbf{r}})}{\partial t} + \sum_{j=1}^N \frac{\partial(\eta_j^* e^{-i2\mathbf{k}_j \cdot \mathbf{r}})}{\partial t} d\mathbf{r} \approx \frac{\partial \eta_j}{\partial t}. \quad (2.9)$$

Only the term containing η_j gives non-zero contribution using the approximation in (2.6), the other terms are zero, since they are multiplied by a periodic function.

Performing the same operation on the right-hand term of (2.3) yields

$$\frac{\partial \eta_j}{\partial t} = \mathcal{L}_j \frac{\delta F_{\eta_j}}{\delta \eta_j^*}, \quad (2.10)$$

where $\mathcal{L}_j = \nabla^2 + 2i\mathbf{k}_j \cdot \nabla - |\mathbf{k}_j|^2$.

Remark 2.2. To simplify the calculation, we employ a long-wavelength limit [44], which allows us to ignore the high-order derivative terms ∇^2 and $2i\mathbf{k}_j \cdot \nabla$ in \mathcal{L}_j . As the wave number $\mathbf{k} \rightarrow 0$, the following result holds

$$\lim_{\mathbf{k} \rightarrow 0} \frac{1}{\varepsilon^d} \int_{C_\varepsilon} (\nabla^2 + 2i\mathbf{k}_j \cdot \nabla) \hat{\eta}_j e^{i\mathbf{k}_j \cdot \frac{\mathbf{r}}{\varepsilon}} d\mathbf{x} = 0, \quad (2.11)$$

where $\hat{\eta}_j$ denote the fourier coefficient of η_j . For the simplicity of presentation, we leave the proof of (2.11) in the Appendix B.3.

From the Remark 2.2, we can set

$$\mathcal{L}_j \approx -|\mathbf{k}_j|^2. \quad (2.12)$$

Hence, the dynamic equation of the APFC model (2.10) can be written as

$$\frac{\partial \eta_j}{\partial t} = -|\mathbf{k}_j|^2 \frac{\delta F_{\eta_j}}{\delta \eta_j^*}, \quad (2.13)$$

where

$$\frac{\delta F_{\eta_j}}{\delta \eta_j^*} = [B_0 + B_x(\nabla^2 + 2i\mathbf{k}_j \cdot \nabla)^2 + 3v(A^2 - |\eta_j|^2)]\eta_j + \frac{\delta f^s}{\delta \eta_j^*}. \quad (2.14)$$

And the free energy functional with respect to η_j is given by

$$F_{\eta_j} = \frac{1}{|\Omega|} \int_{\Omega} \left[\frac{B_0}{2} A^2 + \frac{3v}{4} A^4 + \sum_{j=1}^N (B_x |\varsigma_j \eta_j|^2 - \frac{3v}{2} |\eta_j|^4) + f^s(\eta_j, \eta_j^*) \right] dr, \quad (2.15)$$

where $\varsigma_j := \nabla^2 + 2ik_j \cdot \nabla$. The derivation details of (2.14) and (2.15) are given in the Appendix B.1.

The term A^2 in (2.14) is defined by

$$A^2 := 2 \sum_{j=1}^N |\eta_j|^2. \quad (2.16)$$

It represents a parameter that remains constant within solid and ordered phases but decreases in the presence of defects and interfaces.

The functional $f^s(\eta_j, \eta_j^*)$ corresponds to complex polynomials of η_j and η_j^* , aligned with the appropriate symmetry. In the APFC model (2.13), the crystal lattice symmetry is determined by selecting a suitable set containing N vectors $\{\mathbf{k}_j\}_{j=1}^N$. Below, we present two examples of lattice configurations considered in this work.

Example 2.1. The reciprocal-space vectors used to characterize the crystal symmetry and f^s are determined by the chosen lattice symmetry. For simplicity, we present the results for two types of lattices illustrated in Figure 1, with computational details provided in Appendix B.1.

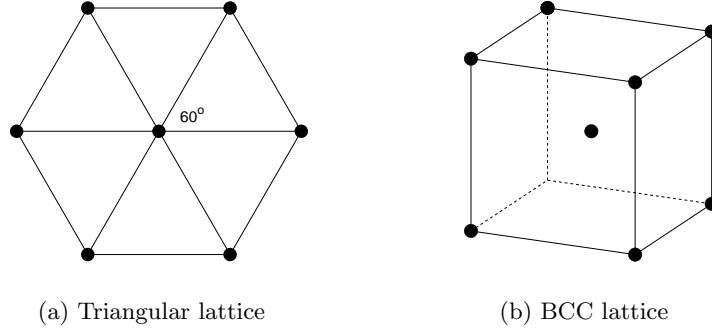


Figure 1: The illustration of unit structures of triangular lattice and BCC lattice.

- For triangular lattice with $N=3$, the complex polynomial functional in (2.14) reads

$$f^s = f_{\text{tri}}^s = -2\tau(\eta_1 \eta_2 \eta_3 + \text{c.c.}),$$

while the derivatives are given by

$$\frac{\delta f_{\text{tri}}^s}{\delta \eta_j^*} = -2\tau \prod_{i \neq j}^3 \eta_i^*, \quad j=1,2,3.$$

- For body-centered cubic (BCC) lattice with $N=6$, the complex polynomial functional in (2.14) reads

$$f^s = f_{\text{bcc}}^s = -2\tau(\eta_1^*\eta_2\eta_3 + \eta_2^*\eta_3\eta_5 + \eta_3^*\eta_1\eta_6 + \eta_4^*\eta_5^*\eta_6^* + \text{c.c.}) \\ + 6v(\eta_1\eta_3^*\eta_4^*\eta_5^* + \eta_2\eta_1^*\eta_5^*\eta_6^* + \eta_3\eta_2^*\eta_6^*\eta_4^* + \text{c.c.}),$$

while the derivatives are given by

$$\frac{\delta f_{\text{bcc}}^s}{\delta \eta_i^*} = -2\tau(\eta_k\eta_n^* + \eta_j\eta_l) + 6v(\eta_k\eta_l\eta_m + \eta_j\eta_m^*\eta_n^*), \\ \frac{\delta f_{\text{bcc}}^s}{\delta \eta_l^*} = -2\tau(\eta_m^*\eta_n^* + \eta_i\eta_j^*) + 6v(\eta_i\eta_k^*\eta_m^* + \eta_k\eta_j^*\eta_n^*),$$

where all the equations for the amplitudes are obtained by permutations on the groups $(i,j,k)=(1,2,3)$ and $(l,m,n)=(4,5,6)$.

3 Numerical Method for the APFC Model

Given the lattice symmetry and periodic boundary conditions, the Fourier pseudospectral method in the spatial direction is well-suited for nonlinear and high-order PDEs due to its high accuracy and straightforward implementation. In Section 3.1, we introduce the basic setup for the Fourier pseudospectral method. Then, in Section 3.2, we provide a detailed explanation of its principles and practical implementation for solving the APFC model (2.13) using Fourier pseudospectral method.

3.1 Basic Setup

In pseudospectral methods, PDEs are solved at collocation points in physical space, where spatial derivatives are computed using orthogonal functions like trigonometric and Chebyshev polynomials. These functions are evaluated using techniques such as matrix multiplication, fast Fourier transform (FFT), or convolution. The Fourier pseudospectral method used in this study follows the procedure outlined in [45], which include selecting collocation points, discretizing the test function by computing the inner product of the equation, obtaining Fourier coefficients, and performing an inverse Fourier transform to obtain the desired function [46].

To that end, given an even integer $N \in \mathbb{N}_0$, we denote

$$K_N^d := \{\mathbf{k} = (k_j)_{j=1}^d \in \mathbb{Z}^d : -\frac{N}{2} \leq k_j < \frac{N}{2}\},$$

where d represents dimension. Let $\mathbb{T}^d := (\mathbb{R}/2\pi\mathbb{Z})^d$ be the d -dimensional torus. We discretize \mathbb{T}^d using the fundamental domain $[0, 2\pi)^d$ with uniform spatial discretization parameter $h = 2\pi/N$. The grid \mathbb{T}_N^d consists of points $\mathbf{r}_{\mathbf{p}} = (x_{1,l_1}, x_{2,l_2}, \dots, x_{d,l_d})$, where $x_{i,l_i} = l_i h$, for $0 \leq l_i < N$, $l_i \in \mathbb{N}_0$.

We define the grid function space

$$\mathcal{G}_N := \{u : \mathbb{T}_N^d \mapsto \mathbb{C} \mid u \text{ is } \mathbb{T}_N^d\text{-periodic}\}.$$

For any periodic grid functions $u, v \in \mathcal{G}_N$, the ℓ^2 -inner product is defined as

$$\langle u, v \rangle_N := \frac{1}{(2\pi N)^d} \sum_{\mathbf{r}_p \in \mathbb{T}_N^d} u(\mathbf{r}_p) v^*(\mathbf{r}_p).$$

For $\mathbf{k}, \mathbf{l} \in \mathbb{Z}^d$, we have the discrete orthogonality condition

$$\langle e^{i\mathbf{k} \cdot \mathbf{r}_p}, e^{i\mathbf{l} \cdot \mathbf{r}_p} \rangle_N = \sum_{\mathbf{r}_p \in \mathbb{T}_N^d} e^{i(\mathbf{k}-\mathbf{l}) \cdot \mathbf{r}_p} = \begin{cases} 1, & \mathbf{k} = \mathbf{l} + N\mathbf{m}, \mathbf{m} \in \mathbb{Z}^d \\ 0, & \text{otherwise} \end{cases}. \quad (3.1)$$

The discrete Fourier coefficient of $u \in \mathcal{G}_N$ is given by

$$\hat{u}_{\mathbf{k}} = \langle u, e^{i\mathbf{k} \cdot \mathbf{r}_p} \rangle_N, \quad \mathbf{k} \in K_N^d.$$

We can also perform the discrete Fourier transform of periodic function u by

$$u(\mathbf{r}_p) = \sum_{\mathbf{k} \in K_N^d} \hat{u}_{\mathbf{k}} e^{i\mathbf{k} \cdot \mathbf{r}_p}, \quad \mathbf{r}_p \in \mathbb{T}_N^d. \quad (3.2)$$

The trigonometric interpolation of periodic function is

$$I_N u(\mathbf{r}) = \sum_{\mathbf{k} \in K_N^d} \hat{u}_{\mathbf{k}} e^{i\mathbf{k} \cdot \mathbf{r}}.$$

It is straightforward to see that $I_N u(\mathbf{r}_p) = u(\mathbf{r}_p)$. In practice, one can use the d -dimensional FFT to obtain the Fourier coefficients $\hat{u}_{\mathbf{k}}$ in (3.2).

Remark 3.1. In addition to the Fourier spectral method discussed above, the finite element method is also commonly used for solving the APFC model [24, 30]. However, it demands more computational resources and requires careful consideration of spatial discretization. For the sake of completeness, we include the implementation details of finite element method in solving the APFC model in Appendix C.

3.2 Implementation of Fourier pseudospectral method

In this section, we give a detailed implementation of solving the APFC model (2.13) by employing Fourier pseudospectral method.

To that end, we first expand the amplitude functions η_j to

$$\eta_j(\mathbf{r}) = \phi_j e^{i\mathbf{k}_j \cdot \mathbf{u}(\mathbf{r})}, \quad j = 1, \dots, N, \quad (3.3)$$

where $\mathbf{u}(\mathbf{r})$ corresponds to the displacement field with respect to the reference lattice [24]. The equations of each η_j are complex functions, and they are independent of each other. Substituting (3.3) into (2.2), one can obtain

$$n(\mathbf{r}) = n_0(\mathbf{r}) + \sum_{j=1}^N [\phi_j e^{i\mathbf{k}_j \cdot \mathbf{r}} e^{i\mathbf{k}_j \cdot \mathbf{u}(\mathbf{r})} + \phi_j e^{-i\mathbf{k}_j \cdot \mathbf{r}} e^{-i\mathbf{k}_j \cdot \mathbf{u}(\mathbf{r})}] \quad (3.4)$$

$$= n_0(\mathbf{r}) + \sum_{j=1}^N [\phi_j e^{i\mathbf{k}_j \cdot (\mathbf{r} + \mathbf{u}(\mathbf{r}))} + \phi_j e^{-i\mathbf{k}_j \cdot (\mathbf{r} + \mathbf{u}(\mathbf{r}))}]. \quad (3.5)$$

In comparison with the density defined by (2.2), we observe that $u(\mathbf{r})$ represents the perturbation term, while $\phi_j e^{i\mathbf{k}_j \cdot \mathbf{r}}$ corresponds to the reference lattice. Here, ϕ_j represents the real value of the amplitude in the relaxed crystal. These quantities can be computed by minimizing the energy functional in (2.1), which is the equilibrium lattice state of the system.

In our work, square and cube are employed as computational domains for two-dimensional and three-dimensional cases, respectively. Let L be the side length of computational domain. The grid points are $\mathbf{r}_p = (\frac{m_1 L}{N}, \frac{m_2 L}{N}) \in \mathbb{T}_N^2$, $0 \leq m_1, m_2 < N$, and $\mathbf{r}_p = (\frac{m_1 L}{N}, \frac{m_2 L}{N}, \frac{m_3 L}{N}) \in \mathbb{T}_N^3$, $0 \leq m_1, m_2, m_3 < N$, $m_i \in \mathbb{N}_0$. The dimensions of K_N^n in different situations are

$$\dim(K_N^n) = N^d =: D, \quad d = 2, 3. \quad (3.6)$$

The amplitude functions η_j are periodic on the Bravais lattice. Based on the relationship between the Bravais lattice and the reciprocal lattice, as well as their mathematical descriptions provided in Appendix A, we can derive their discrete Fourier transform from (A.5) as follows,

$$\eta_j(\mathbf{r}_p, t) \approx I_N^n \eta_j(\mathbf{r}_p, t) = \sum_{\mathbf{k} \in K_N^n} \hat{\eta}_{j\mathbf{k}}(t) e^{i(B\mathbf{k}) \cdot \mathbf{r}_p} \quad p = 0, 1, \dots, N^d - 1,$$

where $\hat{\eta}_{j\mathbf{k}}(t) = \langle \eta_j, e^{i\mathbf{k} \cdot \mathbf{r}_p} \rangle_N$. The first and second order derivative of η_j in Fourier pseudo-spectral method is defined as

$$\begin{aligned} \nabla \eta_j &\approx \sum_{\mathbf{k} \in K_N^n} (B\mathbf{k}) \hat{\eta}_{j\mathbf{k}}(t) e^{i(B\mathbf{k}) \cdot \mathbf{r}_p}, \\ \nabla^2 \eta_j &\approx - \sum_{\mathbf{k} \in K_N^n} |B\mathbf{k}|^2 \hat{\eta}_{j\mathbf{k}}(t) e^{i(B\mathbf{k}) \cdot \mathbf{r}_p}. \end{aligned}$$

Substituting them into the APFC model (2.13), we have

$$\sum_{\mathbf{k} \in K_N^n} \frac{\partial \hat{\eta}_{j\mathbf{k}}(t)}{\partial t} e^{i(B\mathbf{k}) \cdot \mathbf{r}_p} = -|\mathbf{k}_j|^2 \left[\sum_{\mathbf{k} \in K_N^n} \left(B_0 + B_x \left(-(B\mathbf{k})^2 - 2\mathbf{k}_j \cdot (B\mathbf{k}) \right)^2 \right) \hat{\eta}_{j\mathbf{k}}(t) e^{i(B\mathbf{k}) \cdot \mathbf{r}_p} + \hat{G}(\eta) \right],$$

where

$$G(\eta) = G(t, \eta_j(\mathbf{r}_p, t)) := 3v(A^2 - |\eta_j|^2) \eta_j + \frac{\delta f^s}{\delta \eta_j^*}$$

represents the function related to $\eta_1, \dots, \eta_N, \eta_1^*, \dots, \eta_N^*$ and is treated explicitly in the time discretization. By using the basis function $e^{i(B\mathbf{k}) \cdot \mathbf{r}_q}$ to perform the inner product at both ends of the equation simultaneously and applying orthogonality (3.1) yields

$$\frac{\partial \hat{\eta}_{j\mathbf{k}}}{\partial t} = -|\mathbf{k}_j|^2 [B_0 + B_x \left(-(B\mathbf{k})^2 - 2\mathbf{k}_j \cdot (B\mathbf{k}) \right)^2] \hat{\eta}_{j\mathbf{k}}(t) + \hat{G}_{\mathbf{k}}(\eta). \quad (3.7)$$

A semi-implicit scheme is employed for time discretization, allowing us to obtain,

$$\frac{\hat{\eta}_{j\mathbf{k}}^{(n+1)} - \hat{\eta}_{j\mathbf{k}}^{(n)}}{\Delta t} = -|\mathbf{k}_j|^2 [B_0 + B_x \left(-(B\mathbf{k})^2 - 2\mathbf{k}_j \cdot (B\mathbf{k}) \right)^2] \hat{\eta}_{j\mathbf{k}}^{n+1} + \hat{G}_{\mathbf{k}}(\eta^{(n)}).$$

where Δt is the time step size. The iterative format is then given by

$$\hat{\eta}_{j\mathbf{k}}^{(n+1)} = \frac{\hat{\eta}_{j\mathbf{k}}^{(n)} - \Delta t |\mathbf{k}_j|^2 \hat{G}_{\mathbf{k}}(\eta^{(n)})}{1 + \Delta t |\mathbf{k}_j|^2 [B_0 + B_x (-(B\mathbf{k})^2 - 2\mathbf{k}_j \cdot (B\mathbf{k}))^2]}. \quad (3.8)$$

Next, we analyze the computational complexity of solving (3.8) at each time step. The iterative format can be efficiently computed using the Fourier pseudospectral method in d -dimensional reciprocal space. While linear terms are straightforward, the nonlinear terms $\hat{G}(\eta)$ in (3.7) involve computationally intensive convolutions. However, these can be efficiently calculated as dot products in physical space using the Fast Fourier Transform (FFT) [43]. Thus, the complexity of the Fourier pseudospectral method for solving (3.8) is reduced to $\mathcal{O}(D \log D)$ per time step, where D is the number of degrees of freedom defined in (3.6). This method achieves high numerical efficiency and accelerates computations, as will be demonstrated in the following section.

4 Numerical Experiments

In this section, we conduct numerical experiments on both a two-dimensional triangular lattice and a three-dimensional body-centered cubic (BCC) lattice. We introduce quadrupole edge dislocations into the lattice structure with periodic boundary conditions and compute the corresponding variables (e.g., A^2 defined in (2.16)) and the strain field. To further validate the proposed numerical methods, we compare the results with those obtained from continuum elasticity theory of dislocations [47, 48].

4.1 Two-dimensional triangular lattice

We first consider a two-dimensional triangular lattice described in Example 2.1. Let $\phi_j = \phi_0$ represent the amplitude of the equilibrium crystal. By minimizing the energy functional given in (2.15), we obtain ϕ_0 as follows:

$$\phi_0 = \frac{\tau + \sqrt{\tau^2 - 15\nu B_0}}{15\nu}.$$

Further computational details can be found in Appendix B.2. A square computational domain $L_x \times L_y$, with edge lengths $L_x = L_y = 80\pi$, is utilized for numerical simulations. To simulate crystal dislocations, only horizontal shear stress parallel to the x -axis is applied, with no force exerted in the y -direction. The initial condition $\eta_{j,0}$ of the amplitude functions can be determined based on $\eta_j = \phi_0 e^{i\mathbf{k}_j \cdot \mathbf{u}(\mathbf{r})}$ by defining $\mathbf{u}(\mathbf{r})$ as the displacement of the lattice. Given $\mathbf{r} := x\hat{\mathbf{x}} + y\hat{\mathbf{y}}$ as the spatial position vector, the displacement $\mathbf{u}(\mathbf{r})$ is given by:

$$\mathbf{u}(\mathbf{r}) = \begin{cases} -u_x \hat{\mathbf{x}}, & \frac{L_y}{4} < y < \frac{3L_y}{4}, \\ +u_x \hat{\mathbf{x}}, & \text{elsewhere} \end{cases}, \quad (4.1)$$

where $u_x = \frac{a_x}{L_x} x$ with $a_x = \frac{4\pi}{\sqrt{3}}$ and $u_y = 0$. With this choice, a strain of $\varepsilon = \pm \frac{a_x}{L_x}$ is applied to the corresponding region.

We solve the APFC model (2.13) using pseudospectral method, to demonstrate the efficiency of the method, we present the CPU time (in seconds) required to solve the model for various values of N , which represent the degrees of freedom in each direction, as outlined in Section 3.1. The time step size, Δt , is set to 0.1. Table 1 shows the time required for different values of N . The CPU time scales approximately as $O(N^{1.16})$, demonstrating the high efficiency of our model solution process. This efficiency is further underscored by the relatively low computational effort required, as discussed in Section 3.2.

N	32	64	128	256	512	1024
CPU time (s)	0.180	0.462	1.042	1.766	3.320	13.538

Table 1: Triangular lattice: CPU time (s) v.s. N .

4.1.1 Density n and Amplitude Parameter A^2

By solving APFC model (2.13), we can obtain the amplitude functions η_j . These functions can then be used to reconstruct density n by (2.2) and calculate A^2 by (2.16). Figure 2 presents the visualization of the density n defined in (2.2) and the parameter A^2 defined in (2.16), using the parameters $B_0=0.02$, $B_x=0.98$, $v=\frac{1}{3}$, and $\tau=\frac{1}{3}$ from (2.15) as provided in [24]. Figure 2a and Figure 2b display the density n of the perfect lattice and the defect lattice, which can be reconstructed from (2.2). In Figure 2b, the area near the defect is extracted, and the burgers vector can be clearly seen. Figure 2c depicts four blue ellipses representing the regions of defects formed as the system stabilizes, indicating the distribution of dislocations, specifically a quadrupole dislocation. This numerical distribution satisfies the property of the parameter A^2 : it remains constant within ordered phases but decreases in the presence of defects.

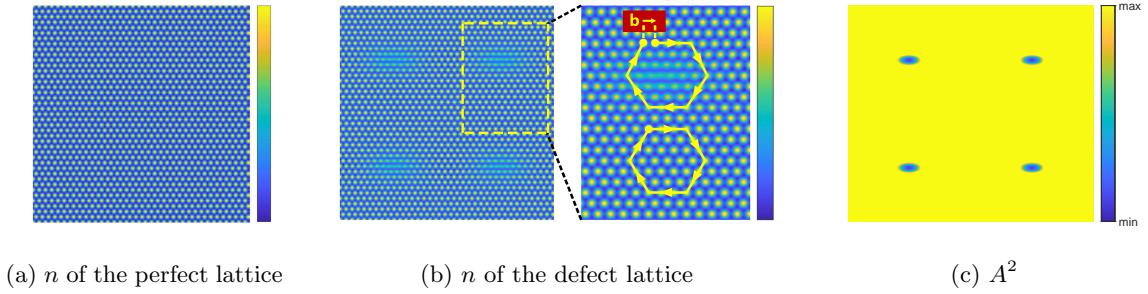


Figure 2: Triangular lattice: The illustration of the density n defined in (2.2) of the perfect lattice and defect lattice, and the parameter A^2 defined in (2.16). Both are colored by values.

Thus, the APFC model effectively retains atomistic features within a continuum framework, functioning as a mesoscale model that connects atomistic and continuum approaches.

4.1.2 Strain Field and Comparison with Continuum Elasticity

To demonstrate the accuracy of the APFC model solutions, we calculate the strain field and compare with continuum elastic theory.

APFC Strain Field: For small deformations, the strain tensor ε can be expressed as

$$\varepsilon = \frac{1}{2} [(\nabla u) + (\nabla u)^T]. \quad (4.2)$$

By solving the APFC model (2.13), we can obtain η_j . The relationship between η_j and u is established by introducing an intermediate variable:

$$\varphi_j = \mathbf{k}_j \cdot \mathbf{u}(\mathbf{r}), \quad j = 1, \dots, N. \quad (4.3)$$

Thus, the equation (3.3) can be written as $\eta_j = \phi_0 e^{i\varphi_j}$. Furthermore, φ_j can be expressed in terms of η_j as follows:

$$\varphi_j = \arg(\eta_j) = \arctan\left(\frac{\text{Im}(\eta_j)}{\text{Re}(\eta_j)}\right), \quad (4.4)$$

where (4.3) defines a system of N linear equations concerning u . We employ the least squares method to solve this system. After some straightforward calculations, the least squares solution of (4.3) in the sense of the Moore-Penrose inverse is expressed as follows,

$$\mathbf{u}(\mathbf{r}) = \begin{cases} u_x = -\frac{\sqrt{3}}{3}\varphi_1 + \frac{\sqrt{3}}{3}\varphi_3, \\ u_y = -\frac{1}{3}\varphi_1 + \frac{2}{3}\varphi_2 - \frac{1}{3}\varphi_3. \end{cases} \quad (4.5)$$

To calculate the strain field according to (4.2), we need to obtain ∇u . Therefore, based on the expression in (4.5), we compute the partial derivatives of φ_j ,

$$\frac{\partial \varphi_j}{\partial \xi} = \frac{1}{|\eta_j|^2} \left[\frac{\partial \text{Im}(\eta_j)}{\partial \xi} \text{Re}(\eta_j) - \frac{\partial \text{Re}(\eta_j)}{\partial \xi} \text{Im}(\eta_j) \right], \quad \xi = x, y. \quad (4.6)$$

Thus, the strain field can be computed solely from η_j , obtained by solving the APFC model (2.13), without the need for additional data. The formulas for the components of the strain field are:

$$\begin{aligned} \varepsilon_{xx} &= -\frac{\sqrt{3}}{3} \frac{\partial \varphi_1}{\partial x} + \frac{\sqrt{3}}{3} \frac{\partial \varphi_3}{\partial x}, \\ \varepsilon_{yy} &= -\frac{1}{3} \frac{\partial \varphi_1}{\partial y} + \frac{2}{3} \frac{\partial \varphi_2}{\partial y} - \frac{1}{3} \frac{\partial \varphi_3}{\partial y}, \\ \varepsilon_{xy} &= -\frac{\sqrt{3}}{3} \frac{\partial \varphi_1}{\partial y} + \frac{\sqrt{3}}{3} \frac{\partial \varphi_3}{\partial y} - \frac{1}{3} \frac{\partial \varphi_1}{\partial x} + \frac{2}{3} \frac{\partial \varphi_2}{\partial x} - \frac{1}{3} \frac{\partial \varphi_3}{\partial x}. \end{aligned} \quad (4.7)$$

Figure 3 illustrates the components of the strain field in a two-dimensional triangular lattice. The distribution of the strain field for a quadrupole dislocation is observed, and

notably, the field distribution at each defect core aligns with theoretical predictions discussed in prior work [39].

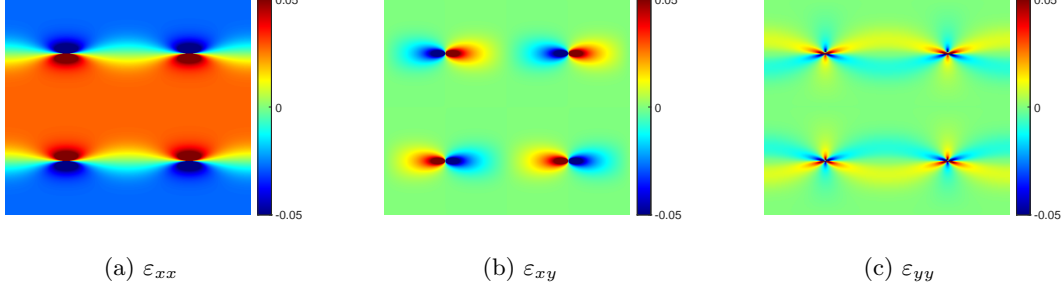


Figure 3: The components of strain field for two-dimensional triangular lattice: (a) ε_{xx} , (b) ε_{xy} and (c) ε_{yy} .

Comparison with Continuum Elasticity Theory We compare the APFC solution with continuum elasticity theory to describe the elastic field of a dislocation [39], assuming that the dislocation characteristics, such as the Burgers vector \mathbf{b} and the elastic constants, are known [49]. Without loss of generality, we set the position of the dislocation core at $\mathbf{x}_c = (0,0)$ and that the Burgers vector \mathbf{b} aligns with the x -axis. To mitigate the singularity inherent at the dislocation core, we adopt the regularization method proposed in [47]. The stress field components can be computed as follows,

$$\begin{aligned}
 \sigma_{xx}/\sigma_0 &= -y(3\zeta^2 + 3x^2 + y^2), \\
 \sigma_{yy}/\sigma_0 &= x(\zeta^2 + x^2 - y^2), \\
 \sigma_{yx}/\sigma_0 &= \sigma_{xy}/\sigma_0 = x(\zeta^2 + x^2 - y^2),
 \end{aligned} \tag{4.8}$$

where

$$\sigma_0 = \frac{E|\mathbf{b}|}{2\pi(1-\nu^2)(\zeta^2 + x^2 + y^2)^2}, \tag{4.9}$$

with $\zeta = |\mathbf{b}|/2$ representing the regularization term, $|\mathbf{b}| = \frac{4\pi}{\sqrt{3}}$, and E and ν representing Young's modulus and Poisson's ratio, respectively.

The strain field can be determined using Hooke's law:

$$\boldsymbol{\varepsilon}^{\text{CE}} = \left[\frac{1+\nu}{E} \right] \boldsymbol{\sigma}^{\text{tot}} - \left(\frac{\nu}{E} \right) \text{tr}(\boldsymbol{\sigma}^{\text{tot}}) \mathbf{I}, \tag{4.10}$$

where σ^{tot} is the total stress field. The strain field in each direction is obtained as follows:

$$\begin{aligned}\varepsilon_{xx} &= \frac{1}{E}(\sigma_{xx} - \nu\sigma_{yy}), \\ \varepsilon_{yy} &= \frac{1}{E}(\sigma_{yy} - \nu\sigma_{xx}), \\ \varepsilon_{xy} &= \frac{1+\nu}{E}\sigma_{xy}.\end{aligned}\tag{4.11}$$

To verify the accuracy, we examine the strain field in three representative directions, as illustrated in Figure 4. These directions are chosen based on the distribution of the strain field. Specifically, we consider the distribution of the strain field ε_{xx} along the directions l_1 and l_2 , and the distribution of ε_{xy} along the direction l_3 . We then compare the strain field in these directions with the theoretical results derived from continuum elasticity theory. Given the symmetry and periodicity of the lattice, it is essential to consider not only the four dislocation cores in the computational domain but also the contributions of dislocations from the surrounding lattice units to the strain field. The periodic extension is performed along the x and y directions, with calculations continuing until reaching the 100th layer. At this point, the error in the strain field between the last two layers is 1×10^{-5} .

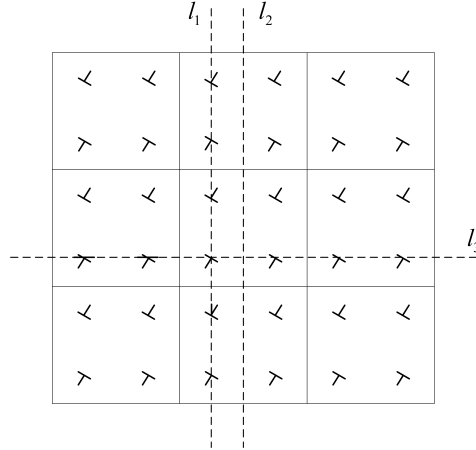


Figure 4: Illustration of periodically repeated domains, where each periodic domain contains a quadrupole edge dislocation.

As shown in Figure 5, the strain field from the APFC model (2.13) is in good agreement with those obtained from continuum elasticity. Notably, we observe variations around the dislocation cores along the l_1 and l_3 directions, which reflects the expected strain field behavior in the presence of dislocations. This demonstrates the effectiveness of the Fourier pseudospectral method in solving the APFC model (2.13), yielding results that closely align with elasticity theory.

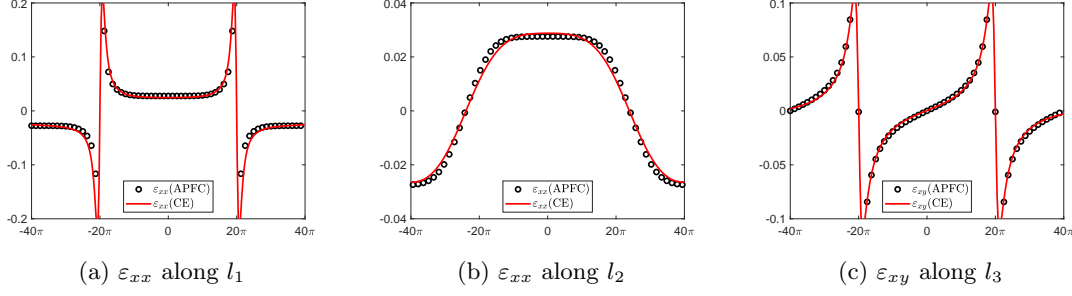


Figure 5: Triangular lattice: Strain fields compared with CE along different lines. The red solid lines represent the results from CE theory, while the black circles represent the results from the APFC model (2.13).

Far Field Decay To verify the accuracy of the Fourier pseudospectral method for solving the APFC model (2.13), we consider a larger computational domain with a side length of 640π . We focus on the case of ε_{xx} in the direction l_1 , noting that the strain field in other directions yields similar results. We demonstrate the results by comparing the decay of ε_{xx} as a function of the distance r from the dislocation core. As shown in Figure 6, both $\varepsilon_{xx}(\text{APFC})$ and $\varepsilon_{xx}(\text{CE})$, representing the results obtained using the APFC model (2.13) and continuum elasticity (CE) theory, respectively, decay like r^{-1} . The error between them decays as r^{-2} , which is consistent with the results shown in [50].

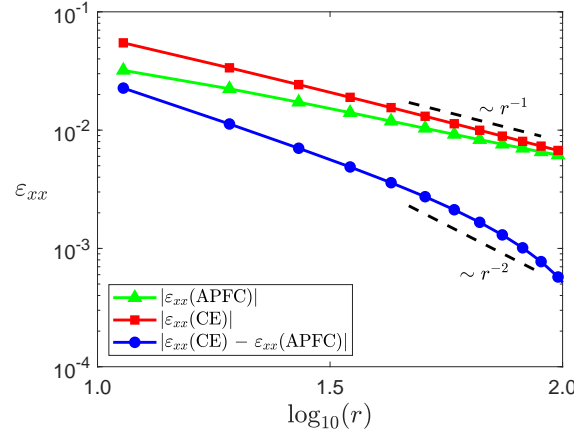


Figure 6: Triangular lattice: The decay of the strain field ε_{xx} along the l_1 direction as a function of the distance r from the dislocation core. The red line represents the results obtained from CE theory, while the green line shows the results from the APFC model (2.13). The blue line represents the error between them.

4.2 Three-dimensional BCC lattice

For the three-dimensional BCC lattice described in Example 2.1, we first let $\phi_j = \phi_0$ represent the amplitude of the equilibrium crystal. By minimizing the energy functional given in (2.15), we obtain ϕ_0 as follows:

$$\phi_0 = \frac{2\tau + \sqrt{4\tau^2 - 45vB_0}}{45v}.$$

Further computational details can be found in Appendix B.2.

A square cube area $L_x \times L_y \times L_z$, with edge length $L_x = L_y = L_z = 60\pi$, is utilized for numerical simulation. To simulate crystal dislocation, shear stress is applied as in the two-dimensional case. Only horizontal shear stress parallel to the xy plane is applied, with no force exerted in the z direction. Based on $\eta_j = \phi_0 e^{i\mathbf{k}_j \cdot \mathbf{u}(\mathbf{r})}$, the initial condition $\eta_{j,0}$ of the amplitude functions can be determined by defining $u(\mathbf{r})$ as a displacement to the lattice. Given $\mathbf{r} := x\hat{\mathbf{x}} + y\hat{\mathbf{y}} + z\hat{\mathbf{z}}$ representing the spatial position vector, the definition of $u(\mathbf{r})$ is then given by:

$$u(\mathbf{r}) = \begin{cases} -u_x \hat{\mathbf{x}} - u_y \hat{\mathbf{y}}, & \frac{L_z}{4} < z < \frac{3L_z}{4}, \\ +u_x \hat{\mathbf{x}} + u_y \hat{\mathbf{y}}, & \text{elsewhere} \end{cases}, \quad (4.12)$$

where $u_x = a_x/L_x x$, $u_y = a_y/L_y y$ and $u_z = 0$ with $a_x = a_y = 2\pi\sqrt{2}$ and L_x, L_y being the length of computational domain. With this choice, a strain of

$$\varepsilon_x = \pm a_x/L_x, \quad \varepsilon_y = \pm a_y/L_y. \quad (4.13)$$

is applied to the corresponding regions.

Table 2 shows the computational time required to solve the model with varying N in the three-dimensional case, using the same time step as in the two-dimensional scenario. Although the computation time has increased, the method retains high efficiency, scaling approximately as $O(N^{2.24})$. It is worth noting that our code has not been optimized; with proper optimization, the CPU computation time could be significantly reduced, leading to even better performance. This further underscores the feasibility of the Fourier pseudospectral method for efficient computations, as discussed in Section 3.2.

N	32	64	128	256	512	1024
CPU time (s)	21.032	62.721	319.545	1854.294	13801.318	31014.621

Table 2: BCC lattice: CPU time (s) v.s. N .

4.2.1 Density n and Amplitude Parameter A^2

We employ the same parameters used in Section 4.1 to solve the APFC model (2.13). Based on how we apply the initial values, we study the distribution of the parameter A^2 defined in (2.16) on the planes $z = L_z/4$ and $z = 3L_z/4$. The distributions on these planes are similar; thus, we present the case for the $z = L_z/4$ plane without loss of generality.

Figure 7 visualizes the density n on the yz -plane with $x = L_x/4$ and the parameter A^2 on the $z = L_z/4$ plane, illustrating the distribution of dislocations as the system stabilizes. Figure 7a and Figure 7b display the density n of the perfect lattice and the defect lattice, which can be reconstructed from (2.2). Similar to the two-dimensional situation, the area near the defect is extracted in Figure 7b, and the burgers vector can be clearly seen. We focus on the regions where A^2 decreases in Figure 7c. The navy blue area corresponds to the region where $A^2 < 0.8\max(A^2)$, indicating the presence of defects as A^2 significantly decreases. The distribution in the figure demonstrates the property of the parameter A^2 : it remains constant within ordered phases but decreases in the presence of defects.

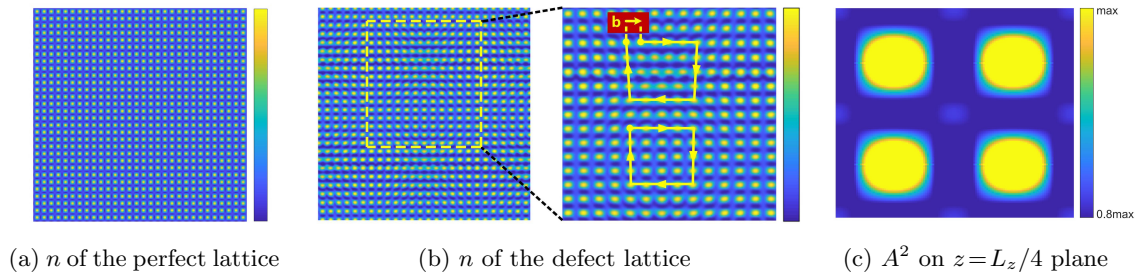


Figure 7: BCC lattice: The illustration of the density n defined in (2.2) for the perfect lattice and defect lattice, and the parameter A^2 on the $z = L_z/4$ plane. Both are colored by their respective values.

4.2.2 Comparison of the Strain Field with Continuum Elasticity Theory

We employ the least squares method to solve the system (4.3). After some straightforward calculations, the least squares solution of (4.3) in the context of the Moore-Penrose inverse is expressed as follows,

$$u(\mathbf{r}) = \begin{cases} u_x = \frac{\sqrt{2}}{4}(\varphi_1 + \varphi_2 + \varphi_5 - \varphi_6) \\ u_y = \frac{\sqrt{2}}{4}(\varphi_1 + \varphi_3 + \varphi_4 - \varphi_5) \\ u_z = \frac{\sqrt{2}}{4}(\varphi_2 + \varphi_3 - \varphi_4 + \varphi_6) \end{cases} . \quad (4.14)$$

Strain Field According to the shear stress applied in (4.13) and the defect distribution shown in Figure 7, we choose to study the strain field distribution on the xz -plane and yz -plane. Given the symmetric structure of the BCC lattice, their distributions should be the same. Without loss of generality, we consider the strain field on the yz -plane with $x = L_x/4$. Similar to the two-dimensional case, the strain field ε_{yz} can be computed using the following formulation:

$$\varepsilon_{yz} = \frac{\sqrt{2}}{8} \left[\left(\frac{\partial \varphi_1}{\partial y} + \frac{\partial \varphi_3}{\partial y} + \frac{\partial \varphi_4}{\partial y} - \frac{\partial \varphi_5}{\partial y} \right) + \left(\frac{\partial \varphi_2}{\partial z} + \frac{\partial \varphi_3}{\partial z} - \frac{\partial \varphi_4}{\partial z} + \frac{\partial \varphi_6}{\partial z} \right) \right].$$

Figure 8 shows the strain field ε_{yz} for the three-dimensional BCC lattice. On this plane, we observe parallel dislocations, and the distribution of the field at each defect core aligns with the theoretical expectations discussed in prior work [39].

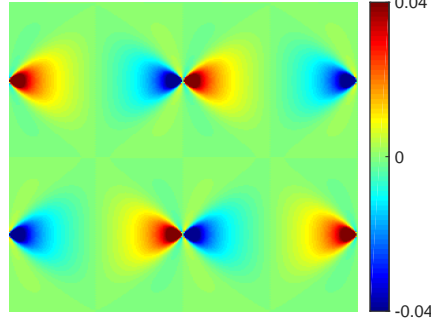


Figure 8: BCC lattice: The illustration of ε_{yz} .

Comparison with CE To verify the accuracy of the APFC solution, we examine the strain field ε_{yz} along the $z=L_z/4$ direction on the yz -plane and compare the strain field from the APFC model (2.13) with the theoretical results derived from continuum elasticity theory.

In the three-dimensional case, based on the distribution of defects shown in Figure 7, we need to consider two sets of dislocations, with both dislocation cores located at $\mathbf{x}_c=(0,0,0)$ and the Burgers vectors perpendicular to each other, aligned parallel to the \mathbf{x} -axis and \mathbf{y} -axis, respectively. Similar to the two-dimensional case, the strain field ε_{yz} can be obtained as follows:

$$\varepsilon_{yz} = \frac{1+\nu}{E} \sigma_{yz}. \quad (4.15)$$

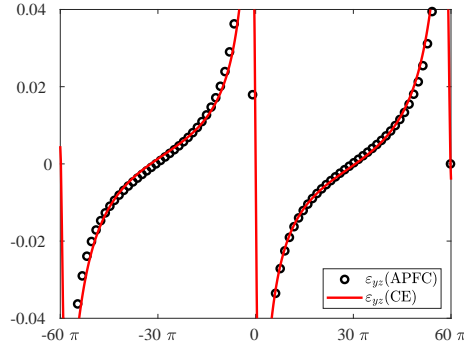


Figure 9: BCC lattice: Strain field ε_{yz} compared with CE along the $z=L_z/4$ direction on the yz -plane. The red solid lines represent the results from CE theory, while the black circles represent the results from the APFC model (2.13).

As shown in Figure 9, the strain field obtained from the APFC model (2.13) closely matches those derived from continuum elasticity (CE). Notably, there is significant numerical variation around the dislocation cores, which is consistent with the expected strain field behavior in these regions. This outcome reaffirms the effectiveness of the Fourier pseudospectral method in solving the three-dimensional APFC model (2.13), producing results that align well with continuum elasticity theory.

Far Field Decay Similar to the two-dimensional case, we consider a larger computational domain with a side length of 640π to verify the accuracy and computational efficiency of the numerical method for solving the APFC model (2.13), as well as to verify the decay of the strain field away from the dislocation core. We demonstrate the results by comparing the decay of ε_{yz} in terms of the distance r from the dislocation core. As illustrated in Figure 10, both the strain field $\varepsilon_{yz}(\text{APFC})$ and $\varepsilon_{yz}(\text{CE})$, corresponding to the APFC model (2.13) and CE theory, exhibit a decay behavior proportional to r^{-1} . Moreover, the error between them decays with a rate of r^{-2} . This behavior mirrors the trends observed in the two-dimensional case, underscoring the robust accuracy of our numerical method in effectively solving the APFC model (2.13).

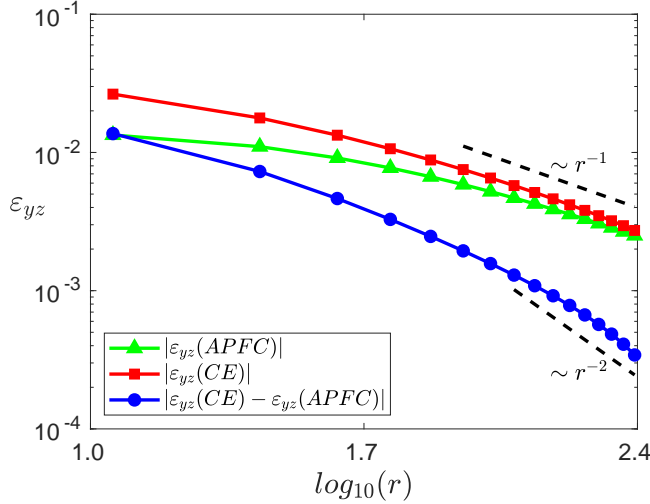


Figure 10: BCC lattice: The decay of the strain field ε_{yz} along $z=L_z/4$ direction on the yz -plane in terms of the distance r from the dislocation core. The red line represents the results from the CE theory while the green line shows the results by using the APFC model (2.13). Moreover, the blue line represents the error between them.

5 Conclusion

In this paper, we have demonstrated the Fourier pseudospectral method for solving the APFC model in dislocation simulations. By leveraging the system's inherent periodicity and applying periodic boundary conditions, the Fourier pseudospectral method

offers exceptional accuracy and computational efficiency. Our numerical experiments on two-dimensional triangular lattices and three-dimensional body-centered cubic lattices successfully optimized edge dislocation geometries, yielding strain fields consistent with continuum elasticity theory predictions. These results highlight the potential of this method in advancing the simulation of complex crystalline defects. Our findings suggest broad applicability of this numerical approach to other crystalline defects, several open problems warrant further investigation:

- Grain-boundary dynamics: Extending the APFC model to grain boundary problems by incorporating a rotation matrix within amplitude functions could enable the simulation of grain boundary evolution. This extension, crucial for studying deformation and rotation in polycrystalline systems, will be a focus of our future work.
- Closing the gap between the APFC and atomistic models: Aligning the elastic parameters of the APFC and atomistic models is key to establishing a connection between them. Future research should explore coupling methods similar to classical atomistic-to-continuum techniques to effectively bridge these models [50].
- Uncertainty quantification of the APFC model: Uncertainty quantification (UQ) is essential in computational materials science to enhance model reliability and guide experimental design. For the APFC model, understanding how parameter uncertainties impact predictions of material properties will be critical, especially when complex structures emerge from varying initial conditions.
- Machine learning in the APFC model: The APFC model encompasses parameters that necessitate calibration for accurately reproducing experimental observations. One promising approach is to utilize machine learning techniques to develop a precise and robust model for the phase field crystal model, facilitating the prediction of crystal structures and enhancing our comprehension of material defect states.

Acknowledgements

XW, YW and LZ are partially supported by NSFC grant 12271360. KJ is partially supported by the National Key R&D Program of China 2023YFA1008802, the National Natural Science Foundation of China 12171412, the Science and Technology Innovation Program of Hunan Province 2024RC1052 and the Innovative Research Group Project of Natural Science Foundation of Hunan Province of China 2024JJ1008. YW is also partially supported by the Development Postdoctoral Scholarship for Outstanding Doctoral Graduates from Shanghai Jiao Tong University. LZ is also partially supported by the Shanghai Municipal Science and Technology Project 22JC1401600 and the Fundamental Research Funds for the Central Universities.

A Introduction to Bravais Lattice and Reciprocal Lattice

In this section, we provide an introduction to Bravais lattices and reciprocal lattices, as well as their mathematical formulations. For any d -dimensional periodic structure $F(\mathbf{r})$, where $\mathbf{r} \in \mathbb{R}^d$, the repeated structural unit is called a unit cell. A fundamental unit cell Ω is described by d vectors ($\mathbf{e}_1, \mathbf{e}_2, \dots, \mathbf{e}_d$):

$$\Omega = \left\{ x \in \Omega \left| x = \sum_{j=1}^n \alpha_j \mathbf{e}_j, \alpha_j \in [0, 1] \right. \right\}. \quad (\text{A.1})$$

The Bravais lattice vector is defined as

$$\mathbf{R}_n = n_1 \mathbf{e}_1 + n_2 \mathbf{e}_2 + \dots + n_d \mathbf{e}_d, \quad n_i \in \mathbb{Z},$$

where $\mathbf{n} = (n_1, n_2, \dots, n_d)$ is a d -dimensional vector. Given the primitive vectors ($\mathbf{e}_1, \mathbf{e}_2, \dots, \mathbf{e}_d$), the reciprocal vectors ($\mathbf{e}_1^*, \mathbf{e}_2^*, \dots, \mathbf{e}_d^*$) satisfy the equation:

$$\mathbf{e}_i \cdot \mathbf{e}_j^* = 2\pi \delta_{ij}.$$

The reciprocal space lattice is given by:

$$\mathbf{G}_m = m_1 \mathbf{e}_1^* + m_2 \mathbf{e}_2^* + \dots + m_d \mathbf{e}_d^*, \quad m_i \in \mathbb{Z},$$

where $\mathbf{m} = (m_1, m_2, \dots, m_d)$ is a d -dimensional integer vector.

One of the most important properties of the reciprocal lattice vector is that the plane wave $\{e^{i\mathbf{G}_m \cdot \mathbf{r}}\}$ can form a set of basis functions for any periodic function $f \in L^2(\mathbb{T}_N^d)$ [51]. This can be expressed as:

$$f(\mathbf{r}) = \sum_{\mathbf{m}} \hat{f}_{\mathbf{m}} e^{i\mathbf{G}_m \cdot \mathbf{r}}. \quad (\text{A.2})$$

For any \mathbf{R}_n in the Bravais lattice, the structure is invariant under lattice translation:

$$f(\mathbf{r} + \mathbf{R}_n) = f(\mathbf{r}). \quad (\text{A.3})$$

Expanding the functions on both sides of equation (A.3) as in equation (A.2), we have:

$$\sum_{\mathbf{m}} \hat{f}_{\mathbf{m}} e^{i\mathbf{G}_m \cdot \mathbf{r}} = \sum_{\mathbf{m}} \hat{f}_{\mathbf{m}} e^{i\mathbf{G}_m \cdot (\mathbf{r} + \mathbf{R}_n)} = \sum_{\mathbf{m}} \hat{f}_{\mathbf{m}} e^{i\mathbf{G}_m \cdot \mathbf{r}} e^{i\mathbf{G}_m \cdot \mathbf{R}_n}.$$

Note that $e^{i\mathbf{G}_m \cdot \mathbf{R}_n} = 1$ holds only if the following equation is satisfied:

$$\mathbf{G}_m \cdot \mathbf{R}_n = 2\pi N, \quad N \in \mathbb{Z}. \quad (\text{A.4})$$

Hence, equation (A.2) can be rewritten as:

$$\begin{aligned} f(\mathbf{r}) &= \sum_{\mathbf{m}} \hat{f}_{\mathbf{m}} e^{i\mathbf{G}_m \cdot \mathbf{r}} \\ &= \sum_{\mathbf{k} \in K_N^n} \hat{f}_{\mathbf{k}} e^{i\left(\frac{2\pi}{\mathbf{R}_n} \cdot \mathbf{k}\right) \cdot \mathbf{r}} \\ &= \sum_{\mathbf{k} \in K_N^n} \hat{f}_{\mathbf{k}} e^{i(B\mathbf{k}) \cdot \mathbf{r}}, \end{aligned} \quad (\text{A.5})$$

where $B = \frac{2\pi}{\mathbf{R}_n}$ is the transformation matrix from physical space to reciprocal space.

B Auxiliary Results

B.1 The derivation of (2.14)

We first derive (2.14). We start by calculating A^2 and A^4 :

$$\begin{aligned} A^2 &= 2 \sum_{j=1}^N |\eta_j|^2 = 2 \sum_{j=1}^N \eta_j \eta_j^*, \\ A^4 &= 4 \left(\sum_{j=1}^N |\eta_j|^2 \right)^2 = 4 \left(\sum_{j=1}^N \eta_j \eta_j^* \right)^2. \end{aligned}$$

Substituting these into (2.15), we obtain

$$\begin{aligned} F_{\eta_j} &= \frac{1}{|\Omega|} \int_{\Omega} \left[\frac{B_0}{2} A^2 + \frac{3v}{4} A^4 + \sum_{j=1}^N \left(B_x |\varsigma_j \eta_j|^2 - \frac{3v}{2} |\eta_j|^4 \right) + f^s(\eta_j, \eta_j^*) \right] d\mathbf{r} \\ &= \frac{1}{|\Omega|} \int_{\Omega} \left[B_0 \sum_{j=1}^N |\eta_j|^2 + 3v \left(\sum_{j=1}^N \eta_j \eta_j^* \right)^2 + \sum_{j=1}^N \left(B_x |\varsigma_j \eta_j|^2 - \frac{3v}{2} |\eta_j|^4 \right) + f^s(\eta_j, \eta_j^*) \right] d\mathbf{r}. \end{aligned} \tag{B.1}$$

The i -th partial functional derivative $\frac{\delta F}{\delta \eta_j^*}$ of F with respect to η_j can be calculated as follows. For any test function $\phi_j \in U$, where U is a Banach space of functions η_j on the computational domain $\Omega \in \mathbb{R}^d$, we have

$$\begin{aligned} \left(\frac{\delta F}{\delta \eta_j^*}, \phi_j \right) &= \frac{d}{dt} F(\eta_1, \dots, \eta_N, \eta_1^*, \dots, \eta_N^*) \Big|_{t=0} \\ &= \lim_{t \rightarrow 0} \frac{F(\eta_1, \dots, \eta_N, \eta_1^*, \dots, \eta_j^* + t\phi_j, \dots, \eta_N^*) - F(\eta_1, \dots, \eta_N, \eta_1^*, \dots, \eta_N^*)}{t} \\ &= \lim_{t \rightarrow 0} \frac{1}{t|\Omega|} \int_{\Omega} \left[B_0 t \eta_j \phi_j + 3v \left((A^2 - \eta_j \eta_j^*) + \eta_j t \phi_j \right) (t \eta_j \phi_j) + B_x t \varsigma_j^2 \eta_j \phi_j - \frac{3v}{2} t \eta_j^2 \phi_j^2 \right] d\mathbf{r} + \left(\frac{\delta f^s}{\delta \eta_j^*}, \phi_j \right) \\ &= \frac{1}{|\Omega|} \int_{\Omega} \left[B_0 \eta_j \phi_j + 3v (A^2 - |\eta_j|^2) \eta_j \phi_j + B_x \varsigma_j^2 \eta_j \phi_j \right] d\mathbf{r} + \left(\frac{\delta f^s}{\delta \eta_j^*}, \phi_j \right) \\ &= ([B_0 + 3v(A^2 - |\eta_j|^2) + B_x \varsigma_j^2] \eta_j, \phi_j) + \left(\frac{\delta f^s}{\delta \eta_j^*}, \phi_j \right). \end{aligned}$$

According to the fundamental lemma of the calculus of variations, for any ϕ_j ,

$$\left(\frac{\delta F}{\delta \eta_j^*}, \phi_j \right) = ([B_0 + B_x(\nabla^2 + 2i\mathbf{k}_j \cdot \nabla) + 3v(A^2 - |\eta_j|^2)] \eta_j, \phi_j) + \left(\frac{\delta f^s}{\delta \eta_j^*}, \phi_j \right).$$

Thus, we obtain

$$\frac{\delta F}{\delta \eta_j^*} = [B_0 + B_x(\nabla^2 + 2i\mathbf{k}_j \cdot \nabla) + 3v(A^2 - |\eta_j|^2)] \eta_j + \frac{\delta f^s}{\delta \eta_j^*}. \tag{B.2}$$

B.1.1 The reciprocal-space vectors and $\delta f^s / \delta \eta_j^*$ defined in the Example 2.1

In Example 2.1, the reciprocal-space vectors used to characterize the crystal symmetry and $\frac{\delta f^s}{\delta \eta_j^*}$ are provided according to the selected lattice symmetry as follows:

1. For two-dimensional triangular lattices with $N=3$, the reciprocal-space vectors are

$$\mathbf{k}_1 = \left(-\frac{\sqrt{3}}{2}, -\frac{1}{2} \right), \quad \mathbf{k}_2 = (0, 1), \quad \mathbf{k}_3 = \left(\frac{\sqrt{3}}{2}, -\frac{1}{2} \right).$$

The complex polynomial functional in (2.14) is given by

$$f_{\text{tri}}^s = -2\tau(\eta_1\eta_2\eta_3 + \text{c.c.}).$$

Following the derivation process of $\frac{\delta F}{\delta \eta_j^*}$, we take $j=1$ as an example:

$$\begin{aligned} \left(\frac{\delta f_{\text{tri}}^s}{\delta \eta_1^*}, \phi_1 \right) &= \frac{d}{dt} f^{\text{tri}}(\eta_1, \eta_2, \eta_3, \eta_1^* + t\phi_1, \eta_2^*, \eta_3^*) \Big|_{t=0} \\ &= \lim_{t \rightarrow 0} \frac{f^{\text{tri}}(\eta_1, \eta_2, \eta_3, \eta_1^* + t\phi_1, \eta_2^*, \eta_3^*) - f^{\text{tri}}(\eta_1, \eta_2, \eta_3, \eta_1^*, \eta_2^*, \eta_3^*)}{t} \\ &= \lim_{t \rightarrow 0} -\frac{2\tau}{t} \frac{1}{|\Omega|} \int_{\Omega} (\eta_1\eta_2\eta_3 + (\eta_1^* + t\phi_1)\eta_2^*\eta_3^* - \eta_1\eta_2\eta_3 - \eta_1^*\eta_2^*\eta_3^*) d\mathbf{r} \\ &= \lim_{t \rightarrow 0} -\frac{2\tau}{t} \frac{1}{|\Omega|} \int_{\Omega} \eta_2^*\eta_3^* t\phi_1 d\mathbf{r} \\ &= (-2\tau\eta_2^*\eta_3^*, \phi_1). \end{aligned}$$

Thus, we find

$$\frac{\delta f_{\text{tri}}^s}{\delta \eta_1^*} = -2\tau\eta_2^*\eta_3^*.$$

In general,

$$\frac{\delta f_{\text{tri}}^s}{\delta \eta_j^*} = -2\tau \prod_{i \neq j}^3 \eta_i^*, \quad j=1, 2, 3. \quad (\text{B.3})$$

2. For the body-centered cubic (BCC) lattice with $N=6$, the reciprocal-space vectors are

$$\begin{aligned} \mathbf{k}_1 &= (1, 1, 0), \quad \mathbf{k}_2 = (1, 0, 1), \quad \mathbf{k}_3 = (0, 1, 1), \\ \mathbf{k}_4 &= (0, 1, -1), \quad \mathbf{k}_5 = (1, -1, 0), \quad \mathbf{k}_6 = (-1, 0, 1). \end{aligned}$$

The complex polynomial functional in (2.14) is given by

$$\begin{aligned} f_{\text{bcc}}^s &= -2\tau(\eta_1^*\eta_2\eta_3 + \eta_2^*\eta_3\eta_5 + \eta_3^*\eta_1\eta_6 + \eta_4^*\eta_5^*\eta_6^* + \text{c.c.}) \\ &\quad + 6v(\eta_1\eta_3^*\eta_4^*\eta_5^* + \eta_2\eta_1^*\eta_5^*\eta_6^* + \eta_3\eta_2^*\eta_6^*\eta_4^* + \text{c.c.}). \end{aligned}$$

Following a similar derivation process for $\frac{\delta F}{\delta \eta_j^*}$, we take η_1^* as an example:

$$\begin{aligned}
\left(\frac{\delta f^{\text{bcc}}}{\delta \eta_1^*}, \phi_1 \right) &= \frac{d}{dt} f^{\text{bcc}}(\eta_1, \eta_2, \dots, \eta_6, \eta_1^* + t\phi_1, \eta_2^*, \dots, \eta_6^*) \Big|_{t=0} \\
&= \lim_{t \rightarrow 0} \frac{f^{\text{bcc}}(\eta_1, \eta_2, \dots, \eta_6, \eta_1^* + t\phi_1, \eta_2^*, \dots, \eta_6^*) - f^{\text{bcc}}(\eta_1, \eta_2, \dots, \eta_6, \eta_1^*, \eta_2^*, \dots, \eta_6^*)}{t} \\
&= \lim_{t \rightarrow 0} -\frac{2\tau}{t} \frac{1}{|\Omega|} \int_{\Omega} (\eta_2 \eta_4 t\phi_1 + \eta_3 \eta_6^* t\phi_1) d\mathbf{r} \\
&\quad + \lim_{t \rightarrow 0} \frac{6v}{t} \frac{1}{|\Omega|} \int_{\Omega} (\eta_2 \eta_5^* \eta_6^* t\phi_1 + \eta_3 \eta_4 \eta_5 t\phi_1) d\mathbf{r} \\
&= \frac{1}{|\Omega|} \int_{\Omega} (-2\tau(\eta_2 \eta_4 + \eta_3 \eta_6^*) + 6v(\eta_2 \eta_5^* \eta_6^* + \eta_3 \eta_4 \eta_5)) \phi_1 d\mathbf{r}.
\end{aligned}$$

Thus, we find

$$\frac{\delta f^{\text{bcc}}}{\delta \eta_1^*} = -2\tau(\eta_2 \eta_4 + \eta_3 \eta_6^*) + 6v(\eta_2 \eta_5^* \eta_6^* + \eta_3 \eta_4 \eta_5).$$

In general,

$$\frac{\delta f^{\text{bcc}}}{\delta \eta_i^*} = -2\tau(\eta_k \eta_n^* + \eta_j \eta_l) + 6v(\eta_k \eta_l \eta_m + \eta_j \eta_m^* \eta_n^*). \quad (\text{B.4})$$

For $\eta_4^*, \eta_5^*, \eta_6^*$, taking η_4^* as an example:

$$\begin{aligned}
\left(\frac{\delta f^{\text{bcc}}}{\delta \eta_4^*}, \phi_4 \right) &= \frac{d}{dt} f^{\text{bcc}}(\eta_1, \eta_2, \dots, \eta_6, \eta_1^*, \dots, \eta_4^* + t\phi_4, \dots, \eta_6^*) \Big|_{t=0} \\
&= \lim_{t \rightarrow 0} \frac{f^{\text{bcc}}(\eta_1, \eta_2, \dots, \eta_6, \eta_1^*, \dots, \eta_4^* + t\phi_4, \dots, \eta_6^*) - f^{\text{bcc}}(\eta_1, \eta_2, \dots, \eta_6, \eta_1^*, \eta_2^*, \dots, \eta_6^*)}{t} \\
&= \frac{1}{|\Omega|} \int_{\Omega} (-2\tau(\eta_5^* \eta_6^* \phi_4 + \eta_1 \eta_2^* \phi_4) + 6v(\eta_1 \eta_3^* \eta_5^* \phi_4 + \eta_3 \eta_2^* \eta_6^* \phi_4)) d\mathbf{r} \\
&= (-2\tau(\eta_5^* \eta_6^* + \eta_1 \eta_2^*) + 6v(\eta_1 \eta_3^* \eta_5^* + \eta_3 \eta_2^* \eta_6^*), \phi_4).
\end{aligned}$$

Thus, we find

$$\frac{\delta f^{\text{bcc}}}{\delta \eta_4^*} = -2\tau(\eta_5^* \eta_6^* + \eta_1 \eta_2^*) + 6v(\eta_1 \eta_3^* \eta_5^* + \eta_3 \eta_2^* \eta_6^*).$$

In general,

$$\frac{\delta f^{\text{bcc}}}{\delta \eta_l^*} = -2\tau(\eta_m^* \eta_n^* + \eta_i \eta_j^*) + 6v(\eta_i \eta_k^* \eta_m^* + \eta_k \eta_j^* \eta_n^*). \quad (\text{B.5})$$

In this case, all the equations for the amplitudes in (B.4) and (B.5) are obtained by permutations of the groups $(i, j, k) = (1, 2, 3)$ and $(l, m, n) = (4, 5, 6)$.

B.2 The calculation of ϕ_0

Let $\phi_j = \phi_0$ represent the amplitude of the equilibrium crystal. By assuming the amplitudes for all η_j to be real and equal, we can set $\eta_j = \phi_0$. This can be determined by minimizing the energy functional given in (2.15).

1. For two-dimensional triangular lattices with $N=3$,

$$f^s = f_{\text{tri}}^s = -2\tau(\eta_1\eta_2\eta_3 + \text{c.c.}).$$

At this point, F_{η_j} defined by (B.1) becomes

$$F_{\eta_j} = \frac{1}{|\Omega|} \int_{\Omega} \left(\frac{45}{2} \phi_0^4 - 4\tau \phi_0^3 + 3B_0 \phi_0^2 \right) d\mathbf{r}. \quad (\text{B.6})$$

According to the mean value theorem, the minimum value is obtained when

$$\phi_0 = \frac{\tau + \sqrt{\tau^2 - 15\nu B_0}}{15\nu}. \quad (\text{B.7})$$

2. For the body-centered cubic (BCC) lattice with $N=6$,

$$\begin{aligned} f^s = f_{\text{bcc}}^s = & -2\tau(\eta_1^* \eta_2 \eta_3 + \eta_2^* \eta_3 \eta_5 + \eta_3^* \eta_1 \eta_6 + \eta_4^* \eta_5^* \eta_6^* + \text{c.c.}) \\ & + 6\nu(\eta_1 \eta_3^* \eta_4^* \eta_5^* + \eta_2 \eta_1^* \eta_5^* \eta_6^* + \eta_3 \eta_2^* \eta_6^* \eta_4^* + \text{c.c.}). \end{aligned}$$

At this point, F_{η_j} defined by (B.1) becomes

$$F_{\eta_j} = \frac{1}{|\Omega|} \int_{\Omega} (135\phi_0^4 - 16\tau\phi_0^3 + 6B_0\phi_0^2) d\mathbf{r}. \quad (\text{B.8})$$

According to the mean value theorem [52], the minimum value is obtained when

$$\phi_0 = \frac{2\tau + \sqrt{4\tau^2 - 45\nu B_0}}{45\nu}. \quad (\text{B.9})$$

B.3 Proofs of the Remarks in Section 2

In this section, we provide the detailed proofs of the Remarks presented in Section 2.
Proof of Remark 2.1.

$$\begin{aligned} \left| \frac{1}{\varepsilon^d} \int_{C_\varepsilon} \eta(\mathbf{x}) e^{i\mathbf{k}_j \cdot \frac{\mathbf{x}}{\varepsilon}} d\mathbf{x} - \frac{1}{\varepsilon^d} \int_{C_\varepsilon} I_\eta e^{i\mathbf{k}_j \cdot \frac{\mathbf{x}}{\varepsilon}} d\mathbf{x} \right| &= \left| \int_{C_1} (\eta(\varepsilon\mathbf{y}) - I_\eta) e^{i\mathbf{k}_j \cdot \mathbf{y}} d\mathbf{y} \right| \\ &\leq \left| \left(\int_{C_1} |\eta(\varepsilon\mathbf{y}) - I_\eta|^2 d\mathbf{y} \right)^{\frac{1}{2}} \left(\int_{C_1} |e^{i\mathbf{k}_j \cdot \mathbf{y}}|^2 d\mathbf{y} \right)^{\frac{1}{2}} \right| \\ &= \left| \left(\int_{C_1} |\eta(\varepsilon\mathbf{y}) - I_\eta|^2 d\mathbf{y} \right)^{\frac{1}{2}} \right| \\ &= \left| \left(\frac{1}{\varepsilon^d} \int_{C_\varepsilon} |\eta(\mathbf{x}) - \frac{1}{\varepsilon^d} \int_{C_\varepsilon} \eta(\mathbf{x}) d\mathbf{x}|^2 d\mathbf{x} \right)^{\frac{1}{2}} \right| \\ &\leq \left| K_\varepsilon \|\nabla \eta(\mathbf{x})\|_{L^2(C_\varepsilon)} \right| \\ &= O(\varepsilon). \end{aligned}$$

□

Proof of Remark 2.2. For any $\varepsilon > 0$, let $\delta' > 0$ and $\delta > 0$ such that $0 < |\mathbf{k}| < \delta'$ and $0 < |-\mathbf{k}^2 - 2\mathbf{k}_j \cdot \mathbf{k}| < \delta$. Then,

$$\begin{aligned}
\left| \frac{1}{\varepsilon^d} \int_{C_\varepsilon} (\nabla^2 + 2i\mathbf{k}_j \cdot \nabla) \hat{\eta}_j e^{i\mathbf{k} \cdot \frac{\mathbf{x}}{\varepsilon}} d\mathbf{x} \right| &= \left| \int_{C_1} (\nabla^2 + 2i\mathbf{k}_j \cdot \nabla) \hat{\eta}_j e^{i\mathbf{k} \cdot \mathbf{y}} d\mathbf{y} \right| \\
&= \left| \int_{C_1} (-\mathbf{k}^2 - 2\mathbf{k}_j \cdot \mathbf{k}) \hat{\eta}_j e^{i\mathbf{k} \cdot \mathbf{y}} d\mathbf{y} \right| \\
&\leq \left| \left(\int_{C_1} |(-\mathbf{k}^2 - 2\mathbf{k}_j \cdot \mathbf{k}) \hat{\eta}_j|^2 d\mathbf{y} \right)^{\frac{1}{2}} \left(\int_{C_1} |e^{i\mathbf{k} \cdot \mathbf{y}}|^2 d\mathbf{y} \right)^{\frac{1}{2}} \right| \\
&= \left| \left(\frac{1}{\varepsilon^d} \int_{C_\varepsilon} |(-\mathbf{k}^2 - 2\mathbf{k}_j \cdot \mathbf{k}) \hat{\eta}_j|^2 d\mathbf{x} \right)^{\frac{1}{2}} \right| \\
&\leq \left| K_\varepsilon (-\mathbf{k}^2 - 2\mathbf{k}_j \cdot \mathbf{k}) \|\nabla \hat{\eta}_j\|_{L^2(C_\varepsilon)} \right| \\
&< \left| K_\varepsilon \delta \|\nabla \hat{\eta}_j\|_{L^2(C_\varepsilon)} \right| \\
&= O(\varepsilon).
\end{aligned}$$

□

C Finite Element Methods for Solving (2.13)

Although we use the Fourier pseudospectral method to solve the APFC model in this work, we include a brief overview of the commonly used finite element method for completeness. This overview, based on previous studies [24, 30, 53, 54], focuses on spatial discretization and adaptivity techniques. For the discretization of the equation (2.13), a conforming triangulation \mathcal{T}_h of the computational domain Ω is considered, usually with simplex elements $S \in \mathcal{T}_h$ of characteristic size h . In the simulation of APFC, linear elements are adopted. Considering a (\mathbb{P}_1) FEM space, we define

$$\mathcal{V}_h^1 = \{v \in \mathbb{C}(\Omega, \mathbb{R}) : v|_S \in \mathbb{P}_1(S, \mathbb{R}), S \in \mathcal{T}_h\}.$$

A function $y \in \mathcal{V}_h^1$ can be expressed in terms of a basis expansion: $y = \sum_i Y_i e_i$, with real coefficients Y_i and basis $\{e_i\}$ of \mathcal{V}_h^1 . A key feature of the FEM approach is splitting equation (2.13) into two second-order equations for $\partial \eta_j / \partial t$ and $\rho_j = \varsigma_j \eta_j$:

$$\begin{aligned}
\frac{\partial \eta_j}{\partial t} &= -|\mathbf{k}_j|^2 \left(B_x \varsigma_j \rho_j + B_0 \eta_j + 3v(A^2 - |\eta_j|^2) \eta_j + \frac{\partial f_s}{\partial \eta_j^*} \right), \\
\rho_j &= \varsigma_j \eta_j = \nabla^2 \eta_j + 2i\mathbf{k}_j \cdot \nabla \eta_j.
\end{aligned} \tag{C.1}$$

Considering that the amplitude functions are complex-valued, we may use complex coefficients with real basis functions. The functions are split into real and imaginary parts and divided accordingly for numerical solution. The following array of functions is considered: $\alpha = [\text{Re}(\eta_1), \text{Im}(\eta_1), \dots, \text{Re}(\eta_p), \text{Im}(\eta_p)]$, $p = 1, \dots, 2N$. The problem to

solve then reads: for $t \in [0, T]$, find $\eta_j = \alpha_k + i\alpha_{k+1}$ and $\varsigma_j \eta_j = \zeta_k + i\zeta_{k+1}$, $k = 2j - 1$, with $\alpha_k, \alpha_{k+1}, \zeta_k, \zeta_{k+1} \in \mathcal{V}_h^1$, such that

$$\begin{aligned}
\frac{\partial \alpha_k}{\partial t} &= -|\mathbf{k}_j|^2 \left[B_0 \alpha_k + B_x (\nabla^2 \zeta_k - 2\mathbf{k}_j \cdot \nabla \zeta_{k+1}) \right. \\
&\quad \left. + 3v (A^2 - |\eta_j|^2) \alpha_k + \operatorname{Re} \left(\frac{\delta f_s}{\delta \eta_j^*} \right) \right], \\
\frac{\partial \alpha_{k+1}}{\partial t} &= -|\mathbf{k}_j|^2 \left[B_0 \alpha_{k+1} + B_x (\nabla^2 \zeta_{k+1} + 2\mathbf{k}_j \cdot \nabla \zeta_k) \right. \\
&\quad \left. + 3v (A^2 - |\eta_j|^2) \alpha_{k+1} + \operatorname{Im} \left(\frac{\delta f_s}{\delta \eta_j^*} \right) \right], \\
\zeta_k &= \nabla^2 \alpha_k - 2\mathbf{k}_j \cdot \nabla \alpha_{k+1}, \\
\zeta_{k+1} &= \nabla^2 \alpha_{k+1} + 2\mathbf{k}_j \cdot \nabla \alpha_k.
\end{aligned} \tag{C.2}$$

The time derivatives are approximated by $\partial \alpha_k / \partial t = (a_k^{n+1} - a_k^n) / \Delta t_n$ and $\partial \zeta_k / \partial t = (\zeta_k^{n+1} - \zeta_k^n) / \Delta t_n$, with $\Delta t_n = t_{n+1} - t_n$ being the time step, and $n \in \mathbb{N}_0$ the index labeling time steps. The time discretization is achieved through a semi-implicit scheme, where the linear terms in (C.2) are evaluated implicitly and the nonlinear terms explicitly.

Notice that N coupled systems must be solved concurrently, with N being the number of independent amplitudes according to the considered lattice symmetry. The adopted semi-implicit integration scheme in matrix form reads:

$$\mathbf{L} \cdot \mathbf{x} = \mathbf{R},$$

with

$$\mathbf{L} = \begin{bmatrix} -\nabla^2 & \mathcal{A} & 1 & 0 \\ -\mathcal{A} & -\nabla^2 & 0 & 1 \\ G_1(\{\alpha_i^{(n)}\}) & 0 & \mathcal{K} \nabla^2 & -\mathcal{K} \mathcal{A} \\ 0 & G_2(\{\alpha_i^{(n)}\}) & \mathcal{K} \mathcal{A} & \mathcal{K} \nabla^2 \end{bmatrix}, \tag{C.3}$$

$$\mathbf{x} = \begin{bmatrix} \alpha_k^{(n+1)} \\ \alpha_{k+1}^{(n+1)} \\ \zeta_k^{(n+1)} \\ \zeta_{k+1}^{(n+1)} \end{bmatrix}, \quad \mathbf{R} = \begin{bmatrix} 0 \\ 0 \\ H_1(\{\alpha_i^{(n)}\}) \\ H_2(\{\alpha_i^{(n)}\}) \end{bmatrix}, \tag{C.4}$$

where $\mathcal{A} = 2\mathbf{k}_j \cdot \nabla$ and $\mathcal{K} = |\mathbf{k}_j|^2 B_x$. The functions evaluated explicitly at time t_n are

given by

$$\begin{aligned}
G_1(\{\alpha_i\}) &= \frac{1}{\tau_n} + |\mathbf{k}_j|^2 B_0 + 3v|\mathbf{k}_j|^2 (A^2 + \alpha_k^2 - \alpha_{k+1}^2), \\
G_2(\{\alpha_i\}) &= \frac{1}{\tau_n} + |\mathbf{k}_j|^2 B_0 + 3v|\mathbf{k}_j|^2 (A^2 + \alpha_{k+1}^2 - \alpha_k^2), \\
H_1(\{\alpha_i\}) &= \left[\frac{1}{\tau_n} + 6|\mathbf{k}_j|^2 v \alpha_k^2 \right] \alpha_k - |\mathbf{k}_j|^2 \operatorname{Re} \left(\frac{\delta f_s}{\delta \eta_j^*} \right), \\
H_2(\{\alpha_i\}) &= \left[\frac{1}{\tau_n} + 6|\mathbf{k}_j|^2 v \alpha_{k+1}^2 \right] \alpha_{k+1} - |\mathbf{k}_j|^2 \operatorname{Im} \left(\frac{\delta f_s}{\delta \eta_j^*} \right).
\end{aligned} \tag{C.5}$$

Furthermore, spatial adaptivity can be adopted to improve the efficiency of numerical simulation. There are many methods to choose from, such as those based on error estimates or indicators. Due to the presence of defects, the amplitude functions may oscillate differently. Based on this property, numerical methods have been developed that focus on the oscillation of the complex amplitudes. We find the region where the quantity $\|\nabla A^2\|_F$ exceeds an arbitrary threshold, where $\|\cdot\|_F$ denotes the Frobenius norm. The method then considers a refinement of the computational grid to ensure proper characterization of all the η_j functions.

References

- [1] P. Lagerlof. Crystal dislocations: Their impact on physical properties of crystals. *Crystals*, 8(11), 2018.
- [2] J. P. Sethna, M. K. Bierbaum, K. A. Dahmen, C. P. Goodrich, J. R. Greer, L. X. Hayden, J. P. Kent-Dobias, E. D. Lee, D. B. Liarte, X. Ni, K. N. Quinn, A. Raju, D. Z. Rocklin, A. Shekhawat, and S. Zapperi. Deformation of crystals: Connections with statistical physics. *Annual Review of Materials Research*, 47(1):217–246, 2017.
- [3] Yangshuai Wang, Shashwat Patel, and Christoph Ortner. A theoretical case study of the generalization of machine-learned potentials. *Computer Methods in Applied Mechanics and Engineering*, 422:116831, 2024.
- [4] Julian Braun, Christoph Ortner, Yangshuai Wang, and Lei Zhang. Higher order far-field boundary conditions for crystalline defects. *arXiv preprint arXiv:2210.05573*, 2022.
- [5] Huajie Chen, Christoph Ortner, and Yangshuai Wang. Qm/mm methods for crystalline defects. part 3: machine-learned mm models. *Multiscale Modeling & Simulation*, 20(4):1490–1518, 2022.
- [6] J Lepinoux and LP Kubin. Dynamic organization of dislocation structures: A simulation. *Scr. Metall.:(United States)*, 21(6), 1987.

- [7] Nasr M Ghoniem and R Amodeo. Computer simulation of dislocation pattern formation. *Solid State Phenomena*, 3:377–388, 1988.
- [8] Robert E Rudd and Jeremy Q Broughton. Coarse-grained molecular dynamics and the atomic limit of finite elements. *Physical review B*, 58(10):R5893, 1998.
- [9] Soumil Y Joshi and Sanket A Deshmukh. A review of advancements in coarse-grained molecular dynamics simulations. *Molecular Simulation*, 47(10-11):786–803, 2021.
- [10] Karin Lin and DC Chrzan. Kinetic monte carlo simulation of dislocation dynamics. *Physical Review B*, 60(6):3799, 1999.
- [11] Wei Cai, Vasily V Bulatov, Sidney Yip, and Ali S Argon. Kinetic monte carlo modeling of dislocation motion in bcc metals. *Materials Science and Engineering: A*, 309:270–273, 2001.
- [12] K. R. Elder, Mark Katakowski, Mikko Haataja, and Martin Grant. Modeling elasticity in crystal growth. *Phys. Rev. Lett.*, 88:245701, Jun 2002.
- [13] K. R. Elder and Martin Grant. Modeling elastic and plastic deformations in nonequilibrium processing using phase field crystals. *Phys. Rev. E*, 70:051605, Nov 2004.
- [14] K. R. Elder, Nikolas Provatas, Joel Berry, Peter Stefanovic, and Martin Grant. Phase-field crystal modeling and classical density functional theory of freezing. *Phys. Rev. B*, 75:064107, Feb 2007.
- [15] Peter Stefanovic, Mikko Haataja, and Nikolas Provatas. Phase-field crystals with elastic interactions. *Phys. Rev. Lett.*, 96:225504, Jun 2006.
- [16] N. Goldenfeld, B. P. Athreya, and J. A. Dantzig. Renormalization group approach to multiscale simulation of polycrystalline materials using the phase field crystal model. *Phys. Rev. E*, 72:020601, Aug 2005.
- [17] Paul Jreidini, Tatu Pinomaa, Jörg MK Wiezorek, Joseph T McKeown, Anssi Laukkanen, and Nikolas Provatas. Orientation gradients in rapidly solidified pure aluminum thin films: comparison of experiments and phase-field crystal simulations. *Physical review letters*, 127(20):205701, 2021.
- [18] Nana Ofori-Opoku, Jonathan Stolle, Zhi-Feng Huang, and Nikolas Provatas. Complex order parameter phase-field models derived from structural phase-field-crystal models. *Physical review b*, 88(10):104106, 2013.
- [19] Ken R Elder, CV Achim, E Granato, SC Ying, and Tapio Ala-Nissila. Striped, honeycomb, and twisted moiré patterns in surface adsorption systems with highly degenerate commensurate ground states. *Physical Review B*, 96(19):195439, 2017.
- [20] KR Elder, Zhi-Feng Huang, and Nikolas Provatas. Amplitude expansion of the binary phase-field-crystal model. *Physical Review E*, 81(1):011602, 2010.

- [21] V. Heinonen, C. V. Achim, K. R. Elder, S. Buyukdagli, and T. Ala-Nissila. Phase-field-crystal models and mechanical equilibrium. *Phys. Rev. E*, 89:032411, Mar 2014.
- [22] A. Skaugen, L. Angheluta, and J. Viñals. Dislocation dynamics and crystal plasticity in the phase-field crystal model. *Phys. Rev. B*, 97:054113, Feb 2018.
- [23] A. Skaugen, L. Angheluta, and J. Viñals. Separation of elastic and plastic timescales in a phase field crystal model. *Phys. Rev. Lett.*, 121:255501, Dec 2018.
- [24] M. Salvalaglio and R. Backofen. Controlling the energy of defects and interfaces in the amplitude expansion of the phase-field crystal model. *Physical Review E*, 96(2):023301, 2017.
- [25] M. A. Choudhary, J. Kundin, and H. Emmerich. Phase-field crystal modeling of anisotropic material systems of arbitrary poisson’s ratio. *Philosophical Magazine Letters - PHIL MAG LETT*, 92:1–8, 09 2012.
- [26] Marcello De Donno, Lucas Benoit-Maréchal, and Marco Salvalaglio. Amplitude expansion of the phase-field crystal model for complex crystal structures. *Physical Review Materials*, 7(3):033804, 2023.
- [27] Kun Wang, Wenjin Chen, Shifang Xiao, Jun Chen, and Wangyu Hu. Pattern formation under deep supercooling by classical density functional-based approach. *Entropy*, 25(5):708, 2023.
- [28] D.-H. Yeon, Z.-F. Huang, K. Elder, and K. Thornton. Density-amplitude formulation of the phase-field crystal model for two-phase coexistence in two and three dimensions. *Philosophical Magazine*, 90(1-4):237–263, 2010.
- [29] Nikolas Provatas and Ken Elder. *Phase-field methods in materials science and engineering*. John Wiley & Sons, 2011.
- [30] M. Salvalaglio, L. Angheluta, Z.-F. Huang, A. Voigt, K. R. Elder, and J. Viñals. A coarse-grained phase-field crystal model of plastic motion. *Journal of the Mechanics and Physics of Solids*, 137:103856, 2020.
- [31] T. Witkowski, S. Ling, S. Praetorius, and A. Voigt. Software concepts and numerical algorithms for a scalable adaptive parallel finite element method. *Advances in Computational Mathematics*, 41(6):1145–1177, 2015.
- [32] B. P. Athreya, N. Goldenfeld, J. A. Dantzig, M. Greenwood, and N. Provatas. Adaptive mesh computation of polycrystalline pattern formation using a renormalization-group reduction of the phase-field crystal model. *Phys. Rev. E*, 76:056706, Nov 2007.
- [33] M. Berčič and G. Kugler. Adaptive mesh simulations of polycrystalline materials using a cartesian representation of an amplitude expansion of the phase-field-crystal model. *Phys. Rev. E*, 98:033303, Sep 2018.

- [34] Robert Spatschek and Alain Karma. Amplitude equations for polycrystalline materials with interaction between composition and stress. *Phys. Rev. B*, 81:214201, Jun 2010.
- [35] Petri Hirvonen, Mikko M Ervasti, Zheyong Fan, Morteza Jalalvand, Matthew Seymour, S Mehdi Vaez Allaei, Nikolas Provatas, Ari Harju, Ken R Elder, and Tapio Ala-Nissila. Multiscale modeling of polycrystalline graphene: A comparison of structure and defect energies of realistic samples from phase field crystal models. *Physical Review B*, 94(3):035414, 2016.
- [36] Marco Salvalaglio and Ken R. Elder. Coarse-grained modeling of crystals by the amplitude expansion of the phase-field crystal model: an overview. *Modelling and Simulation in Materials Science and Engineering*, 30, 2022.
- [37] Jie Shen, Tao Tang, and Li-Lian Wang. *Spectral methods: algorithms, analysis and applications*, volume 41. Springer Science & Business Media, 2011.
- [38] David Gottlieb and Steven A Orszag. *Numerical analysis of spectral methods: theory and applications*. SIAM, 1977.
- [39] Peter M Anderson, John P Hirth, and Jens Lothe. *Theory of dislocations*. Cambridge University Press, 2017.
- [40] K. R. Elder, N. Provatas, J. Berry, P. Stefanovic, and M. Grant. Phase-field crystal modeling and classical density functional theory of freezing. *Phys.rev.b*, 75(6):794–802, 2007.
- [41] N. Goldenfeld, B. P. Athreya, and J. A. Dantzig. Renormalization group approach to multiscale modelling in materials science. *Journal of Statistal Physics*, 125(5-6):1015–1023, 2006.
- [42] B. P. Athreya, N. Goldenfeld, and J. A. Dantzig. Renormalization group theory for the phase field crystal equation. *Physical Review E*, 74(1):011601, 2006.
- [43] Pingwen Zhang and Xinwei Zhang. An efficient numerical method of landau–brazovskii model. *Journal of Computational Physics*, 227(11):5859–5870, 2008.
- [44] K. R. Elder, Zhi-Feng Huang, and Nikolas Provatas. Amplitude expansion of the binary phase-field-crystal model. *Phys. Rev. E*, 81:011602, Jan 2010.
- [45] Kai Jiang, Shifeng Li, and Pingwen Zhang. Numerical methods and analysis of computing quasiperiodic systems. *SIAM Journal on Numerical Analysis*, 62(1):353–375, 2024.
- [46] J. Shen, T. Tang, and L. L. Wang. *Fourier Spectral Methods for Periodic Problems*. Springer Berlin Heidelberg, 2011.
- [47] W. Cai, A. Arsenlis, and C. R. Weinberger. A non-singular continuum theory of dislocations. *Journal of the Mechanics and Physics of Solids*, 54(3):561–587, 2006.

- [48] Derek Olson, Christoph Ortner, Yangshuai Wang, and Lei Zhang. Elastic far-field decay from dislocations in multilattices. *Multiscale Modeling & Simulation*, 21(4):1379–1409, 2023.
- [49] J. P. Hirth, J. Lothe, and T. Mura. Theory of Dislocations (2nd ed.). *Journal of Applied Mechanics*, 50(2):476–477, 06 1983.
- [50] M. Salvalaglio, A. Voigt, and K. R. Elder. Closing the gap between atomic-scale lattice deformations and continuum elasticity. *Npj Computational Materials*, 5(1), 2019.
- [51] André Authier, Charles Alfred Taylor, Union internationale de cristallographie. Commission on Crystallographic Teaching, and University of Wales (Cardiff). *The reciprocal lattice*. University College Cardiff Press Cardiff, 1981.
- [52] Vladimir Antonovich Zorich and Octavio Paniagua. *Mathematical analysis II*, volume 220. Springer, 2016.
- [53] Yangshuai Wang, Huajie Chen, Mingjie Liao, Christoph Ortner, Hao Wang, and Lei Zhang. A posteriori error estimates for adaptive qm/mm coupling methods. *SIAM Journal on Scientific Computing*, 43(4):A2785–A2808, 2021.
- [54] Christoph Ortner and Yangshuai Wang. A framework for a generalization analysis of machine-learned interatomic potentials. *Multiscale Modeling & Simulation*, 21(3):1053–1080, 2023.